Thermal stability of gold/palladium octopods studied in situ in 3D : understanding design rules for thermally stable metal nanoparticles

Thermal Stability of Gold/Palladium Octopods Studied *In Situ* in 3D: Understanding Design Rules for Thermally Stable Metal Nanoparticles

Wiebke Albrecht,[*,†] Eva Bladt,[†] Hans Vanrompay,[†] Joshua D. Smith,[‡] Sara E. Skrabalak,[‡] and Sara Bals[*,†]

†*EMAT, University of Antwerp, Groenenborgerlaan 171, B-2020 Antwerp, Belgium*

‡*Department of Chemistry, Indiana University, Bloomington, Indiana, United States*

E-mail: Wiebke.Albrecht@uantwerpen.be; Sara.Bals@uantwerpen.be

Abstract

Multifunctional metal nanoparticles (NPs) such as anisotropic multimetallic NPs are crucial for boosting nanomaterial based applications. Advanced synthetic protocols exist to make a large variety of such nanostructures. However, a major limiting factor for the usability of them in real life applications is their stability. Here, we show that Au/Pd octopods, 8-branched nanocrystals with O_h symmetry, with only a low amount of Pd exhibited a high thermal stability and maintained strong plasmon resonances up to 600 °C. Furthermore, we study the influence of the composition, morphology and environment on the thermal stability and define key parameters for the design of thermally stable multifunctional NPs.

Keywords

Au/Pd octopods, *in situ* electron tomography, *in situ* heating, electron energy loss spectroscopy, thermal stability

Metal nanoparticles (NPs) are intriguing systems that are intensely studied because of their broad range of functionalities, which can be exploited in a wide range of applications. For example, due to their efficient interaction with light, involving localized surface plasmon resonances (LSPRs), metal NPs are used in optical and photothermal applications such as sensing,[1] optical data storage,[2] photocatalysis[3] and photovoltaics.[4] Next to optical applications, biocompatible metal NPs such as Au or Pd NPs are promising candidates for biomedical applications[5] and are used as agents for drug delivery[6] and hyperthermic cancer treatment.[7] The list of physical properties, functionalities and applications is tightly bound to the synthesis of novel morphologies and compositions of metal NPs. For example, anisotropic NPs with sharp tips and corners exhibit orders of magnitude stronger field enhancements compared to spherical NPs.[8] Multimetallic NPs can lead to synergistic effects and novel physical or chemical properties.[9]

Due to this dependence of the physical and chemical properties on the morphology and composition of metal NPs, a lot of effort has been put in the synthesis of novel metal NPs.[10,11] As the ability to manipulate the optical properties of metal NPs is mainly limited by the variety of NP shapes,[8,12] most research has focused on understanding design rules for creating novel NP morphologies.[13,14] Over the last decades significant progress has been made and NPs of various shapes and compositions can now be routinely synthesized. Highly anisotropic nanostars,[15] chiral,[16] cage-like[17] or octopodal NPs[18] are just few examples. Especially, stellated NPs have attracted increasing attention due to their sharp tips and consequently strong electric field enhancements and high refractive index sensitivity.[19] Among them Au/Pd octopods have proven to be interesting systems due to a large degree of synthesis control allowing for the tuning of their size, morphology and composition.[18,20] Furthermore, the combination of a strong plasmonic material like Au with a catalytically

active material such as Pd holds promise for many applications such as plasmon enhanced catalysis,[21,22] sensing[23] and surface enhanced Raman scattering (SERS).[24] Au/Pd octopods were especially shown to be highly valuable in sensing due to their large refractive index sensitivity.[18,25]

Whereas synthesis design strategies of NP morphologies have made significant progress,[26] one important factor is often overlooked in these strategies. In order to preserve the carefully designed morphologies and functionalities, the stability of the NPs is of utmost importance. Whereas the chemical stability can be enhanced by employing chemically inert metals such as Au, the thermal stability of metal NPs poses a more serious problem as metal NPs are surprisingly unstable even at temperatures hundreds of degrees Celsius below their melting point. For example, the bulk melting point of Au is 1064 °C but Au NPs exhibit morphological changes at temperatures as low as 100 °C.[27] For laser-based applications temperatures of a few hundred of degrees of Celsius are easily reached, especially if pulsed lasers are used, and laser-induced deformation of metal NPs has been frequently observed.[27–30] Similarly, for applications where higher temperatures are involved such as (photo-)catalysis, metal NPs might deform and lose their properties of interest.

One approach to enhance the thermal stability of metal NPs is the use of coatings that hinder the migration of surface atoms.[31,32] Especially rigid coatings like silica have proven to greatly enhance the (photo)thermal stability of Au NPs.[33–36] However, most coatings significantly hamper the usability of NPs in a large range of applications like catalysis or sensing where the accessibility of the metal surface is a prerequisite. Alternatively, multimetallic systems can enhance the thermal stability compared to monometallic systems without blocking the surface of the NP.[37] For example, by introducing metals with a high melting point such as Pd (1555 °C), NPs made of lower melting point metals like Au can be expected to improve in thermal stability. However, the amount of studies to understand the thermal instability of metal NPs is not at all linked to the fast progress of the synthesis of metal NPs and the thermal stability of more complex shapes or multimetallic NPs has not been intensely researched

so far. While design strategies have been established to carefully control the morphologies of metal NPs, a current challenge is to also determine key factors and design strategies for thermally stable metal NPs that can be employed for long lasting applications of the future.

Most thermal stability studies so far have been performed on large ensembles of metal NPs by monitoring the shift of plasmon resonance upon heating or by making use of 2D electron microscopy techniques such as scanning electron microscopy (SEM) or transmission electron microscopy (TEM).[38–41] However, these approaches are only reliable for symmetric NPs such as nanorods, where direct interpretations can be made about the aspect ratio of the nanorod from the plasmon resonance wavelength or 2D electron microscopy data. For highly complex and anisotropic NPs, conclusions on the 3D morphology and heat-induced morphological changes cannot be unambiguously drawn from 2D projection images or optical techniques. To overcome these limitations, electron tomography is an ideal technique.[42–44] The method uses a series of 2D projection images taken along different tilt angles over a large angular range to reconstruct the 3D morphology and internal structure of the object. Combined with the recent development of *in situ* heating holders that can tilt to high tilt angles, thermal stability studies of complex NPs in 3D become feasible.[45]

Here, we study the thermal stability of Au/Pd octopods by *in situ* heating electron tomography experiments. We determine three key factors that need to be taken into account when designing thermally stable metal NPs: composition, morphology and surrounding environment. First, we show that the addition of Pd to the octopods enhances the thermal stability of the NPs by several hundreds of degrees Celsius. Second, we observe that the curvature of the tips of the octopods plays an important role in the stability. Thirdly, the environment needs to be taken into account when analyzing the thermal stability as heating under inert conditions increases the stability. Finally, we prove by electron energy loss spectroscopy (EELS) that the excellent plasmonic properties of Au can be preserved for a low amount of Pd, while obtaining a high thermal stability.

Results and Discussion

Au/Pd octopods were synthesized by seed-mediated co-reduction, wherein Au and Pd salts are co-reduced in the presence of Au seeds; this procedure allows for control over octopodal size and composition.[18] For comparison, all-Au octopods were prepared by omitting the Pd salt from the synthesis.[12] Full details can be found in the Supporting Information. The thermal stability of the octopods was probed by heating electron tomography.[45] In short, after depositing the sample on a MEMS-based heating chip, high-angle annular dark-field scanning transmission electron microscopy (HAADF-STEM) tomography series of a single octopod were taken before and after several heating steps. During the acquisition of the tomography series the sample was cooled down to 25 °C after each heating step to ensure that the particle did not change while the series were acquired. The heating time for each step was chosen to be 5 min for two reasons. It has been shown that most heat-induced deformation happens within the first minutes.[27,45] Furthermore, by choosing a relatively short heating time the overall experiment time could be reduced allowing for a fine temperature sampling. The tomography series were reconstructed by making use of the ASTRA toolbox implementation of the Expectation-Maximization algorithm.[46,47] Details of the data acquisition and processing are given in the Methods section. In the following we discuss key factors and design strategies for thermally stable metal NPs by varying three parameters during heating: the morphology, composition and environment of the octopods.

Influence of composition on the thermal stability

Figure 1 and Supporting Movie M1 show the outcome of a typical heating tomography experiment performed on a single Au/Pd octopod with a size (distance between opposite branches) of about 150 nm and a Au/Pd atomic percent ratio of approximately 82/18. A tomography series was taken at 25 °C and after heating for 5 min at every 50 °C step between 200 °C and 900 °C. To be able to study a fine temperature sampling and hence many tomography series,

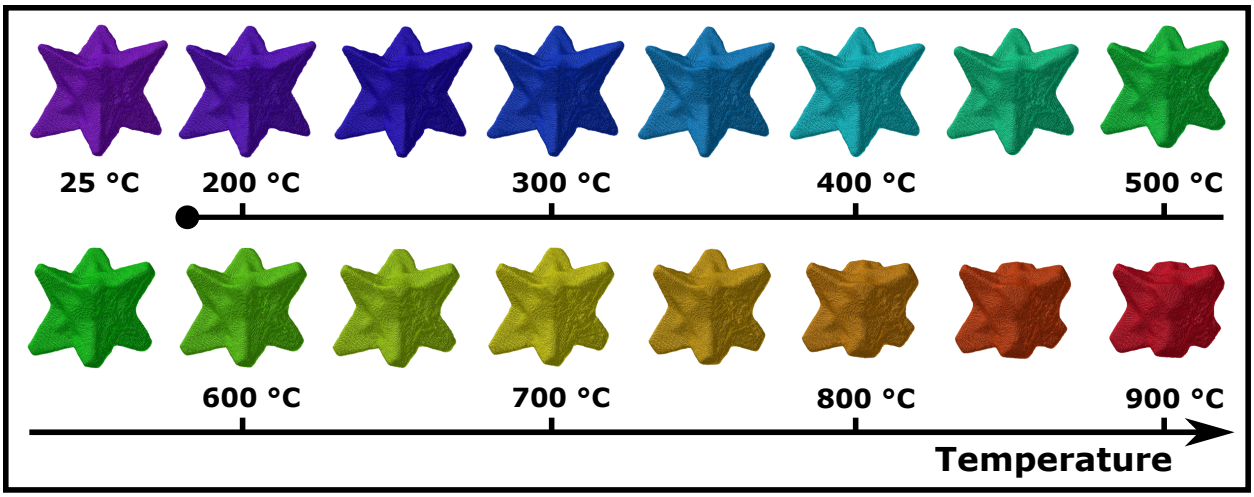

Figure 1: 3D visualization of the same Au/Pd octopod before (25 °C) heating and after heating for 5 min at intermediate temperatures between 200 °C and 900 °C. The octopod is about 150 nm in size (distance between opposite branches) with a Au/Pd at% ratio of 82/18. Morphological changes of all tips are visible in the Supporting Movie M1.

we used a fast tomography approach to acquire the data presented in Figure 1 as recently described elsewhere.[45] By visual inspection of the reconstructions of the octopod at different heating temperatures, it can be observed that the particle shape, including the sharp tips, did not change morphology up to a heating temperature of 450 °C. Above 450 °C the tips deformed with increasing heating temperature.

In order to quantify the observed deformation behaviour, the difference between reconstructions at room temperature and at higher temperatures are calculated. In this manner, the differences in morphology between the initial octopod shape and the heated octopod shape at each temperature are obtained. Details of the procedure can be found in the Experimental section. Figure 2a displays the resulting 3D visualizations of the local volume decrease upon heating superimposed on the 3D visualization of the octopod before heating. Figure 2b presents the local volume increases after heating the octopod at 700 °C and 900 °C for 5 min. From Figure 2 it is clear that the local volume decreases are only located at the tips, whereas the local volume increases are located at the sides of the octopod indicating that atoms diffused from areas of high curvature to areas of low curvature. The calculated difference reconstructions allow to determine the amount of redistributed volume which is

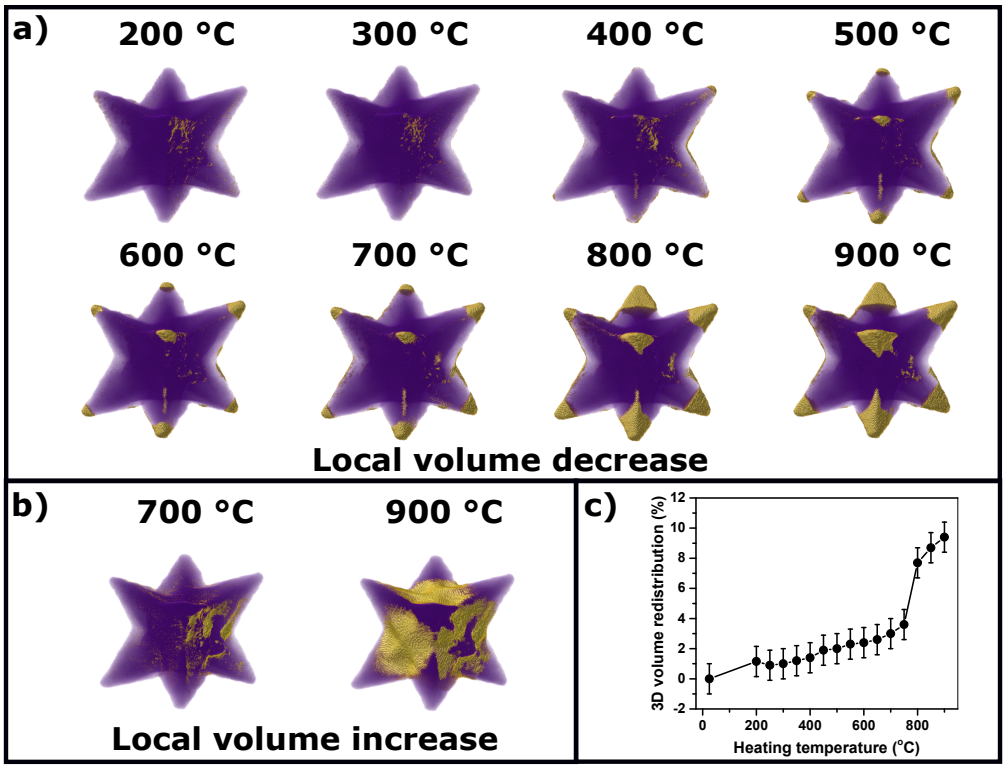

Figure 2: Volume redistribution of the heated octopod from Figure 1. a) 3D visualizations of local volume decreases (golden colour) at different heating temperatures superimposed with the initial octopod morphology (purple). b) 3D visualizations of local volume increases after heating to 700 °C and 900 °C. The full series of local volume increases and decreases for all temperatures is shown in Figure S2. c) Redistributed volume for the same octopod as a function of heating temperature.

plotted in Figure 2c. Up to 750 °C the volume redistribution increased gradually up to 4 %. At higher temperatures the rate of volume redistribution accelerated and after heating at 900 °C almost 10 % of the total volume of the octopod redistributed. We verified that the same trend was observed for other octopods of the same synthesis batch (black curves in Figure S3). While the composition of the heated Au/Pd octopods did not change over the course of a heating experiment (Figure S4a,c), metal redistribution took place upon heating. The unheated octopods exhibited a Pd-enriched shell (Figure S5). Upon heating Au and Pd redistributed and at 800 °C the octopods were fully alloyed (Figure S5). This transition from a Pd-enriched shell to an alloyed particle could be an additional reason for the increasing rate of redistributed volume at higher temperatures. If Pd moves away from the surface, a

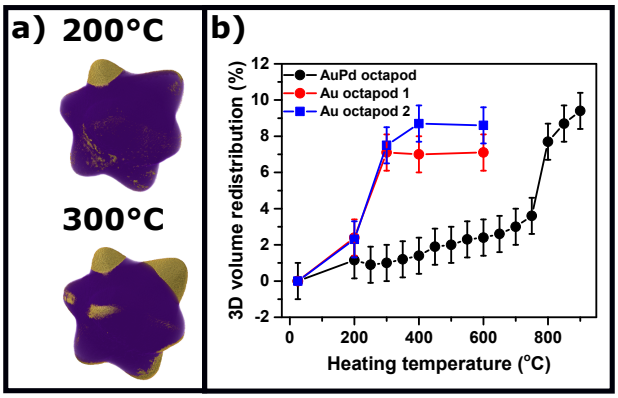

Figure 3: Influence of composition. a) 3D local volume decrease visualizations of a Au only octopod after heating at 200 °C and 300 °C for 5 min. b) Percentage of redistributed volume of two Au octopods (blue and red curves) compared to the Au/Pd octopod from Figure 1 (black curve).

higher content of Au atoms will most likely lead to a higher atom mobility at the surface.

To test how far the addition of Pd enhanced the thermal stability of anisotropic NPs, we first compare the obtained results to the thermal stability of pure Au octopods. As displayed in Figure 3a, a clear deformation of the pure Au octopods was already visible at 200 °C and significant at 300 °C. Figure 3b compares the redistributed volume of the Au/Pd octopod displayed in Figure 2 with the results for two Au octopods. For the Au octopods the initial deformation was 2 times higher at 200 °C and 8 times higher at 300 °C compared to the Au/Pd octopods. At higher temperatures the deformation slowed down and halted. This effect can be most likely attributed to the electron beam induced transformation of the surrounding ligands into a protective carbon shell as observed for other Au NPs.[48] This carbon shell most likely hinders surface diffusion and could be the reason for the slowing down of the deformation of the pure Au octopods. This is supported by the observation that Au octopods, that were not irradiated by the electron beam, lost all prominent morphological features at 200 °C (Figure S14). While it can be concluded that the addition of Pd has a significant influence on the thermal stability of the octopod, the thermal stability did not decrease when lowering the Au/Pd atomic percent ratio to approximately 91:9 (Figure S7a-c). Interestingly, the octopod with 9 at% of Pd exhibited about two times less redistributed

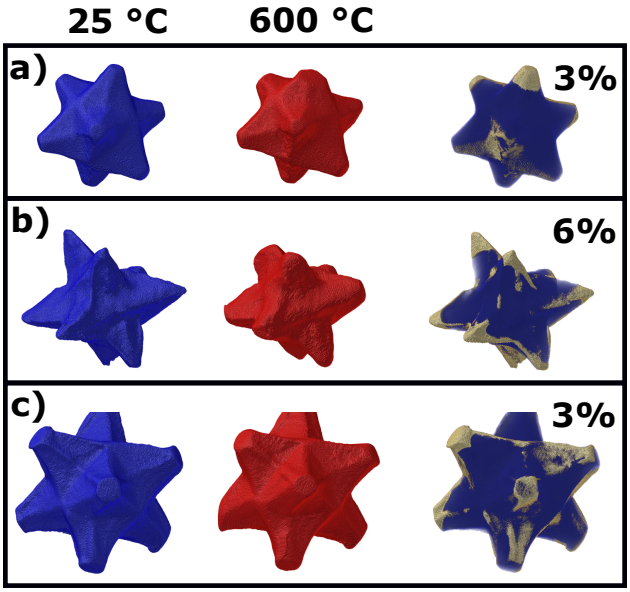

Figure 4: Comparison of the thermal stability of octopods with different morphologies. 3D visualizations before and after heating to 600 °C as well as the local volume decrease of a) an octopod with blunt tips and a Au/Pd atomic percent ratio of 92/8. b) an octopod with sharp tips and a Au/Pd atomic percent ratio of 83/17 of the same volume. c) an octopod with blunt tips and a Au/Pd atomic percent ratio of 90/10 with a 2 times larger volume than the other two octopods. All octopods were heated under the same conditions on the same heating chip.

volume compared to an octopod with 17 at% Pd that was heated on the same chip under the same conditions (Figure S7d-f). This difference might stem from a slight difference in morphology as the octopods originated from two different synthesis batches. Thus, with a addition of only 9 at% of Pd the thermal stability of the octopods can be significantly enhanced compared to Au only octopods.

Influence of morphology on the thermal stability

To study the influence of the sharpness of the octopods' tips in more detail, we compared the thermal stability of an octopod with blunt tips to one with very sharp tips of the same volume ($V = 5.3 \cdot 10^5\,nm^3$). 3D visualizations of these two octopods are presented in Figure 4a and b before heating (left column) and after heating at 600 °C for 5 min (middle column). The right column in Figure 4 displays the difference reconstruction of the octopods before

and after heating. It can be observed that the morphology of the octopod with blunt tips changed less compared to the one with sharp tips resulting in a similar morphology of both octopods after heating. This can also be seen in the quantitative difference of redistributed volume as 6±1 % of volume was redistributed for the octopod with sharp tips whereas only half of that value was redistributed for the octopod with blunt tips.

To evaluate whether volume plays a significant role in the stability, we performed the same experiment on a blunt-tipped octopod with a 2 times larger volume ($V = 1.0 \cdot 10^6\,nm^3$) than the octopod with blunt tips presented in Figure 4a ($V = 0.5 \cdot 10^6\,nm^3$). The results are presented in Figure 4c. Alike to the smaller octopod with blunt tips the larger octopod also barely deformed exhibiting the same volume redistribution as the smaller blunt-tipped octopod. Thus, in this case it can be concluded that a particle with a smaller size but same morphological features is not less stable than a larger particle. This is valid for the size differences studied here and might differ for sizes with orders of magnitude difference. It needs to be noted that the results presented in Figure 4 were obtained under the exact same conditions as both samples were deposited on the same heating chip and hence heated at the same time. Thus, possible differences in temperatures can be excluded and the difference in stability can mostly be attributed to the initial difference in morphology. The octopods with sharp tips are less likely stable since the high curvature of the tips induces surface diffusion of the atoms to lower curvature areas.[30,45] The blunt tips are known to be {111} faceted[49] and the outcome of our experiments suggests that these facets could furthermore enhance the stability.

Influence of environment on the thermal stability

Due to the variety of possible applications for the Au/Pd octopods, the environments in which these particles are used in, can range from inert to oxidizing conditions. Next to shape and composition, the surrounding environment of the nanoparticles can also be expected to play a role in their stability. To compare the inert vacuum conditions to an oxidizing environment

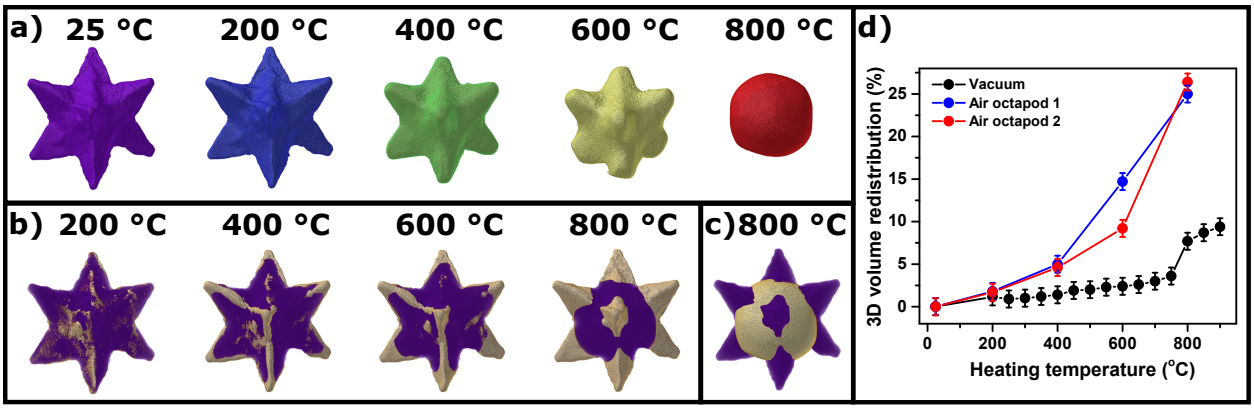

Figure 5: Influence of surrounding environment. a) 3D visualizations of an octopod with sharp tips heated in air. b) 3D visualizations of local volume decreases at different temperatures. c) 3D visualizations of the local volume increase at 800 °C. d) Percentage of redistributed volume for two octopods heated in air (blue and red curve) compared to the octopod of the same sample heated in vacuum from Figure 1 (black curve).

we performed a heating experiment in air. Therefore, we heated a Si_3N_4 heating chip with deposited octopods with sharp tips from the same batch as the octopod in Figure 1 in a static air oven at a desired temperature for 5 min and performed tomography on the same octopod before heating and after every heating step. Figure 5a displays the 3D visualizations of the same octopod heated at 200 °C, 400 °C, 600 °C and 800 °C for 5 min each. The corresponding 3D visualizations of the redistributed volume at each temperature are shown in Figure 5b and c. Similar to the octopods heated in vacuum, the tips deformed first and volume redistributed to areas of lower curvature (Figure 5c). The quantitative comparison of volume redistribution for octopods heated in vacuum (black curves) and air (red and blue curve) is presented in Figure 5d. It can be seen that an increasing rate of distributed volume with increasing heating temperature is also observed for the air heated octopods. However, the rate increase is higher for the air heated octopods at higher temperatures. To specify, for the octopods heated in air the volume distribution was about 4 times higher at temperatures above 400 °C resulting in a complete deformation to a spherical-like shape at 800 °C. We confirmed that the Au/Pd ratio did not change over the course of the experiment (Figure S4b,c) and similarly to the experiment in vacuum, a transition from a Pd-enriched shell to a fully alloyed nanoparticle occurred (Figure S6).

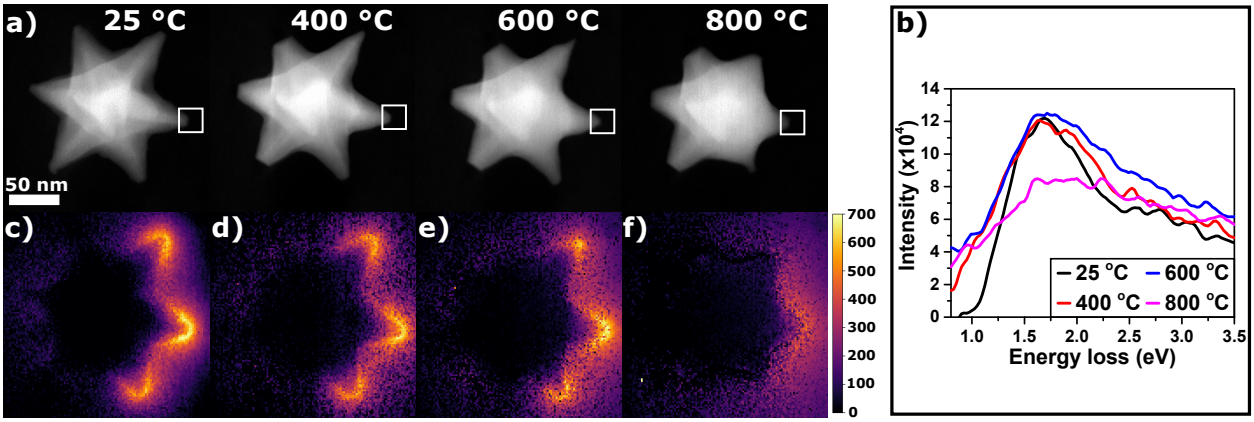

Figure 6: *In situ* heating EELS measurements. a) HAADF-STEM images of the octopod at different heating temperatures. b) Distal LSPR resonance extracted at the middle right tip (marked by white squares in a)). c)-f) Plasmon maps of the distal LSPR resonances at different heating temperatures. The legend for the mapped intensities is shown on the right.

The curvature of anisotropic Au NPs has recently been identified as a key factor in the thermal stability of the particles.[30,45] Taylor *et al.* showed that the main reshaping mechanism of gold nanorods is curvature-driven surface diffusion of atoms and that nanorods with higher aspect ratio and thus higher curvature deform easier than lower curvature nanorods.[30] We recently directly visualized for gold nanostars in 3D that indeed atoms from areas of high curvature diffuse towards areas of low curvature[45] and this reshaping mechanism of curvature-driven surface diffusion is confirmed by our work here. However, from the presented data it becomes clear that morphology is not the only factor that influences the thermal stability.

We identified that the composition of the octopod played a major role in the stability upon heating. The results for the pure Au octopods are expected and in line with previous studies on anisotropic Au NPs. For example, Au NRs were shown to already decrease in aspect ratio after heating at 100 °C for 5 min and fully reshaped to spherical NPs after heating at 250 °C for 30 min.[27] Similarly, the tips of Au nanostars started to deform after heating for 30 s at 200 °C and significantly deformed after heating for 30 s at 300 °C.[45] As can be seen in Figure 3 the Au octopods did not exhibit as sharp tips as the nanostars or the Au/Pd octopods. Yet, they already deformed at 200 °C. In contrast, the Au/Pd octopods

did not show any change in shape up to 450 °C. To some extent it is expected that the addition of Pd leads to a higher thermal stability as Pd has a higher melting temperature (1555 °C) in comparison to Au (1064 °C). Consequently, it has been observed that the melting temperature of Au/Pd nanoparticles increases with increasing Pd content.[50] However, our results show that the addition of only a few percent of Pd is sufficient to tremendously increase the thermal stability compared to Au NPs.

One concern about the addition of Pd is that it might hamper the plasmonic properties as Pd is a material with strong intrinsic damping. However, combined with a superior plasmonic material such as gold, good plasmonic properties of the combined structure can be obtained. For Au/Pd octopods such as the ones studied here, narrow and strongly localized plasmon resonances at the tips were observed.[49] By comparing the distal and nominal LSPR resonances of a Au/Pd with 10 at% of Pd and a Au octopod presented in Figure S10, we confirm that here. Although the LSPR resonances were broader for the Au/Pd octopod due to the presence of interband transitions for Pd resulting in plasmon damping,[49,51] the intensities of the LSPR resonances were as strong as for the Au octopod (Figure S10c). Additionally, the LSPR resonances for the Au/Pd octopod were indeed strongly localized at the sharp tips (Figure S10a).

As mainly the sharp tips deform upon heating and since these are crucial for strong plasmon resonances and plasmonic applications, it is important to investigate the plasmonic properties upon heating. Therefore, we performed *in situ* electron-energy loss spectroscopy (EELS) measurements. Figure 6 summarizes the results for an octopod with sharp tips and a Au/Pd atomic percent ratio of about 84/16 which did not change over the course of heating (Figure S4a,c). Figure 6a displays the HAADF-STEM images of the octopod at 25 °C, 400 °C, 600 °C and 800 °C. These projection images as well as the plasmon maps were taking at a tilt angle of -60 ° as at this angle six out of the eight tips of the particle were visible. Figure 6b displays the measured low loss EELS spectra of the middle right tip (marked by white squares) after zeroloss peak subtraction (see the Experimental section for details). The

observed peak can be attributed to the distal LSPR of the octopod which corresponds to the three right tips that are surrounded by vacuum.[49] The three left tips visible in Figure 6a were touching the Si_3N_4 support which resulted in a damped and red-shifted nominal LSPR (Figure S8b).

Prior to heating the distal LSPR is located around 1.7 eV. This measured resonance is blue-shifted compared to the average ensemble plasmon resonance of the octopod sample with sharp tips which is at 1.4 eV (895 nm, Figure S1) due to a decrease in the surrounding refractive index of the EELS measurements which were performed in vacuum. In Figure 6c it can be seen that the distal mode is strongly localized at the tips of the octopod. A quantitative comparison for the different heating temperatures showed that the distal LSPR resonance barely lost intensity and did not shift significantly upon heating up to 600 °C (red and blue curve in Figure 6b and Figures 6d,e). Only at 800 °C a clear drop in intensity can be observed (magenta curve in Figure 6b and Figure 6f). The results for the nominal LSPR maps are shown in Figure S8c-e. Whereas the distal mode preserved a clear field enhancement localized around the three right tips up to 600 °C, the nominal mode LSPR strength was significantly decreased for two out of the three left tips at 400 °C. This decrease in intensity is mainly attributed to the deformation of the tips. The three right tips (distal LSPR modes) were sharper at 400 °C and 600 °C compared to the three left tips (nominal modes) which naturally results in a stronger field enhancement. A reason for this could be the direct contact of the left tips with the heating support, although this effect was not observed for the tomography experiments presented above. The deformation of the left tips from sharp to blunt tips also led to the observed blue-shift of the nominal LSPR mode (Figure S8b) from 1.2 eV at 25 °C to about 1.7 eV at 800 °C.

Next to the morphology and composition, the surrounding environment in which the particle was heated influenced the stability as well. Octopods of the same synthesis batch and thus with the same composition and shape were more stable when heated in vacuum than in air (Figures 1 and 5). Although the electron beam could enhance the stability during the *in*

situ experiments in vacuum due to the transformation of the ligands into a protective carbon shell as shown for Au NRs,[48] for the Au/Pd octopods this influence seems to be only relevant for heating temperatures above 600 °C (Figures S11 and S12). Interestingly, a similar effect of the electron beam was observed for the octopods heated in air (Figure S13). Additionally, there is likely a temperature discrepancy between the MEMS heating chips and the static air oven as a difference in temperature of about 75 °C - 90 °C between *in situ* TEM and *ex situ* measurements was recently proposed to explain discrepancies in alloying temperatures.[52] Therefore, we confirmed the *in situ* results for different heating chips and the same synthesis batch of octopods with sharp tips and observed the same qualitative trend for all octopods. Despite minor quantitative differences in redistributed volume, all octopods that were heated in vacuum were more stable than the ones heated in air (Figure S3). Furthermore, the shape evolution of the octopods differed for both environments. In vacuum, the highly deformed octopods stayed faceted, whereas in air the octopods deformed to a spherical shape. These results point towards more fundamental differences in the deformation mechanism in air and vacuum most likely involving the burning of the ligands in air. In fact, CTAB is known to decompose at temperatures above 250 °C in air[53] which could explain the accelerated rate of redistributed volume at higher temperatures compared to heating in vacuum.

Conclusions

To conclude, Au/Pd octopods displayed an improved thermal stability preserving their complete morphology up to 450 °C when heated in vacuum. Three main parameters were studied to understand their influence on the thermal stability of the NPs. First, the initial morphology of the octopods influenced their stability as only half of the volume percent, that was redistributed for octopods with sharp tips, redistributed for octopods with blunt tips. Second, at higher temperatures the surrounding environment notably played a role in the stability of the octopods as well and octopods heated in air exhibited 4 times more vol-

ume redistribution compared to octopods heated in vacuum at temperatures above 400 °C. Finally, the addition of only 10 at% of Pd significantly stabilized the octopods as Au only particles already reshaped at 200 °C and showed 8 times stronger volume redistribution at 300 °C. It is interesting to note that, despite the addition of the poor plasmonic metal Pd to the Au/Pd octopods strong field enhancements localized at the tips of the octopods could be observed up to 600 °C making Au/Pd octopods promising candidates for applications where high temperatures are needed.

Experimental

Synthesis of Au/Pd and Au octopods

In a first step, Au octahedra were synthesized by a previously reported hydrothermal method in a 30 mL vial.[54] To obtain the Au/Pd octopods, seed-mediated co-reduction was performed as previously described with modifications.[55] The all Au octopods were prepared by sequential overgrowth of the Au octahedra. While the Au/Pd octopods can be prepared with sharp tips, all-Au octopods with similarly sharp tips have yet to be realized synthetically, presumably because of the higher diffusion rate of Au on Au compared to Pd on Au.[56] Details on the synthesis can be found in the Supporting Information.

In situ electron tomography, heating and EELS

The conventional tilt series for the HAADF-STEM heating tomography were acquired using a FEI Tecnai Osiris electron microscope operated at 200 kV using a DENSsolutions Wildfire tomography heating holder with MEMS-based heating chips. The fast tomography series were obtained at an aberration-corrected cubed FEI-Titan electron microscope operated at 300 kV using the same heating holder. To ensure a larger temperature homogeneity, where possible we chose particles in the middle of the chip, and for a direct comparison, we chose particles that were lying close to each other. The target temperature was reached within

a few seconds and for every chosen temperature the heating time was 5 min after which the sample was cooled back down to 25 °C for the acquisition of the tomography series. The octopods were generally lying in the same orientation on the heating chip with four branches touching the support and the other four branches being surrounded by vacuum. As the thermal conductivity of the metal nanoparticles is high, we do not expect significant temperature gradients in the particle.

For the heating experiments performed in air, a static air furnace was used (Carbolite CWF1300). The octopods were deposited on the same support as for the *in situ* measurements (MEMS heating chip) and placed in the preheated oven and heated for 5 min at the desired temperature.

For the data presented in Figure 1 a fast tomography approach was applied as described elsewhere[45] to obtain a fine temperature sampling. For the rest of the presented data, the series were acquired by taking 49 projection images over an angular range of ± 72° with a tilt increment of 3° with a frame time of 8 s.

To determine the Au/Pd ratios of the octopods, EDX maps were obtained using the Super-X detector of the Tecnai Osiris or FEI Titan electron microscope. The maps were generally acquired for about 10 min at a current of about 150 pA. The EDX data were quantified using the Cliff-Lorimer method. The errors for the quantified Au and Pd content were about 9 at% for Au and 1 at% for Pd.

The EELS measurements were performed at an aberration-corrected cubed FEI-Titan electron microscope operated at 300 kV using the same heating holder. The same heating protocol was used as for the *in situ* tomography experiments and the EELS maps were obtained after cooling down to 25 °C after each heating step. The EELS data analysis was performed with Hyperspy 1.3.2.[57] First, the zeroloss peaks were aligned and then subtracted from the rest of the spectra by fitting a zeroloss peak of a background region as a scalable fixed pattern. To quantify the EELS maps, three spectral contributions were identified. Next to the distal and nominal LSPR mode, the third contribution can be ascribed to interband

transitions (Figure S9).[49] To obtain the spatial distributions of the modes, the three scalable fixed patterns were used as an input for fitting a combination of the three modes to each pixel. In order to quantitatively compare the EELS spectra and maps, a correction factor was applied to the intensity. For that, first the mean intensity of the different spectrum images were obtained before zeroloss peak subtraction. Then, the ratio of the maximum of the mean intensity was used as the correction factor for the intensity making a quantitative comparison between different spectra and maps possible.

Reconstruction of tomography data and data analysis

After alignment of the projection images by using a cross correlation, the stacks of aligned projection images served as inputs for 20 iterations of the Expectation Maximization reconstruction implemented in the ASTRA toolbox.[46,47]

To calculate the difference reconstructions and quantify the redistributed volume, the reconstructions of the experiment of the same octopod at different temperatures were first aligned using intensity based rigid registration.[45] Then, the reconstructions for each octopod were segmented by choosing thresholds for the reconstructions at different temperatures that resulted in the same total volume of the octopod. By performing the alignment and segmentation as described it can be ensured that the difference in reconstructions is representative of local volume increases and decreases. The error of redistributed volume was determined in the following way. First, the redistributed volume was calculated for each pair of reconstructions at consecutive temperatures. Then, these values were compared to the corresponding differences obtained from Figures 2c, 3b and 5d. The discrepancy was generally within $\pm 1\,\%$ which was taken as the error of redistributed volume.

It should be noted that the quantitative comparison between the Au/Pd and Au octopods as well as for the different environments are presented with respect to the Au/Pd octopod heating results presented in Figures 1 and 2. Due to possible temperature inhomogeneities on the heating chip as well as calibration differences for different heating chips, these factors

might change (see Figure S3).

Acknowledgement

W. A. acknowledges an Individual Fellowship funded by the Marie Sklodowska-Curie Actions (MSCA) in Horizon 2020. H. V. acknowledges financial support by the Research Foundation Flanders (FWO grant 1S32617N). E. B. acknowledges a post-doctoral grant from the Research Foundation Flanders (FWO, Belgium). J. D. S. and S.E.S acknowledge funding from the US National Science Foundation (award number: CHE-1602476). The authors acknowledge funding from the European Commission Grant (EUSMI E180600101 to S. B. and S. E. S.) and European Research Council (ERC Starting Grant #335078-COLOURATOMS).

Supporting Information Available

The Supporting Information is available free of charge on the ACS Publications website at DOI: .

- Supporting Information: synthesis details, full series of volume increases and decreases,comparison of Au/Pd octopods on different heating chips, EDX during heating, influence of Au/Pd ratio, additional EELS data, impact of the electron beam
- Supporting Movie: Movie M1 visualizes the changes in morphology upon heating of an Au/Pd octopod in 3D

References

1. Vigderman, L.; Khanal, B. P.; Zubarev, E. R. Functional Gold Nanorods: Synthesis, Self-Assembly, and Sensing Applications. *Adv. Mater.* **2012**, *24*, 4811–4841.

2. Zijlstra, P.; Chon, J. W. M.; Gu, M. Five-Dimensional Optical Recording Mediated by Surface Plasmons in Gold Nanorods. *Nature* **2009**, *459*, 410–413.

3. Linic, S.; Aslam, U.; Boerigter, C.; Morabito, M. Photochemical Transformations on Plasmonic Metal Nanoparticles. *Nat. Mater.* **2015**, *14*, 567–576.

4. Atwater, H. A.; Polman, A. Plasmonics for Improved Photovoltaic Devices. *Nat. Mater.* **2010**, *9*, 205–213.

5. Dreaden, E. C.; Alkilany, A. M.; Huang, X.; Murphy, C. J.; El-Sayed, M. A. The Golden Age: Gold Nanoparticles for Biomedicine. *Chem. Soc. Rev.* **2012**, *41*, 2740–2779.

6. Zhang, Z.; Wang, L.; Wang, J.; Jiang, X.; Li, X.; Hu, Z.; Ji, Y.; Wu, X.; Chen, C. Mesoporous Silica-Coated Gold Nanorods as a Light-Mediated Multifunctional Theranostic Platform for Cancer Treatment. *Adv. Mater.* **2012**, *24*, 1418–1423.

7. Kennedy, L. C.; Bickford, L. R.; Lewinski, N. A.; Coughlin, A. J.; Hu, Y.; Day, E. S.; West, J. L.; Drezek, R. A. A New Era for Cancer Treatment: Gold-Nanoparticle-Mediated Thermal Therapies. *Small* **2011**, *7*, 169–183.

8. Reguera, J.; Langer, J.; Jiménez de Aberasturi, D.; Liz-Marzán, L. M. Anisotropic Metal Nanoparticles for Surface Enhanced Raman Scattering. *Chem. Soc. Rev.* **2017**, *46*, 3866–3885.

9. Cortie, M. B.; Mcdonagh, A. M. Synthesis and Optical Properties of Hybrid and Alloy Plasmonic Nanoparticles. *Chem. Rev.* **2011**, *111*, 3713–3735.

10. Rycenga, M.; Cobley, C. M.; Zeng, J.; Li, W.; Moran, C. H.; Zhang, Q.; Qin, D.; Xia, Y. Controlling the Synthesis and Assembly of Silver Nanostructures for Plasmonic Applications. *Chem. Rev.* **2011**, *111*, 3669–3712.

11. Hou, S.; Hu, X.; Wen, T.; Liu, W.; Wu, X. Core - Shell Noble Metal Nanostructures Templated by Gold Nanorods. *Adv. Mater.* **2013**, *25*, 3857–3862.

12. Smith, A. F.; Weiner, R. G.; Skrabalak, S. E. Symmetry-Dependent Optical Properties of Stellated Nanocrystals. *J. Phys. Chem. C* **2016**, *120*, 20563–20571.

13. Li, N.; Zhao, P.; Astruc, D. Anisotropic Gold Nanoparticles: Synthesis, Properties, Applications, and Toxicity. *Angew. Chem., Int. Ed.* **2014**, *53*, 1756–1789.

14. Polavarapu, L.; Zanaga, D.; Altantzis, T.; Rodal-Cedeira, S.; Pastoriza-Santos, I.; Pérez-Juste, J.; Bals, S.; Liz-Marzán, L. M. Galvanic Replacement Coupled to Seeded Growth as a Route for Shape-Controlled Synthesis of Plasmonic Nanorattles. *J. Am. Chem. Soc.* **2016**, *138*, 11453–11456.

15. Novikov, S. M.; Sánchez-Iglesias, A.; Schmidt, M. K.; Chuvilin, A.; Aizpurua, J.; Grzelczak, M.; Liz-Marzán, L. M. Gold Spiky Nanodumbbells: Anisotropy in Gold Nanostars. *Part. Part. Syst. Charact.* **2014**, *31*, 77–80.

16. Lee, H. E.; Ahn, H. Y.; Mun, J.; Lee, Y. Y.; Kim, M.; Cho, N. H.; Chang, K.; Kim, W. S.; Rho, J.; Nam, K. T. Amino-Acid- and Peptide-Directed Synthesis of Chiral Plasmonic Gold Nanoparticles. *Nature* **2018**, *556*, 360–365.

17. Goris, B.; Polavarapu, L.; Bals, S.; Tendeloo, G. V.; Liz-Marzán, L. M. Monitoring Galvanic Replacement Through Three-Dimensional Morphological and Chemical Mapping. *Nano Lett.* **2014**, *14*, 3220–3226.

18. Desantis, C. J.; Skrabalak, S. E. Size-Controlled Synthesis of Au/Pd Octopods with High Refractive Index Sensitivity. *Langmuir* **2012**, *28*, 9055–9062.

19. Chen, H.; Kou, X.; Yang, Z.; Ni, W.; Wang, J. Shape- and Size-Dependent Refractive Index Sensitivity of Gold Nanoparticles. *Langmuir* **2008**, *24*, 5233–5237.

20. Desantis, C. J.; Skrabalak, S. E. Manipulating the Optical Properties of Symmetrically Branched Au / Pd Nanocrystals Through Interior Design. *Chem. Commun.* **2014**, *50*, 5367–5369.

21. Huang, X.; Li, Y.; Chen, Y.; Zhou, H.; Duan, X.; Huang, Y. Plasmonic and Catalytic AuPd Nanowheels for the Efficient Conversion of Light into Chemical Energy. *Angew. Chem., Int. Ed.* **2013**, *52*, 6063–6067.

22. Zheng, Z.; Tachikawa, T.; Majima, T. Plasmon-Enhanced Formic Acid Dehydrogenation Using Anisotropic Pd - Au Nanorods Studied at the Single-Particle Level. *J. Am. Chem. Soc.* **2015**, *137*, 948–957.

23. Chiu, C. Y.; Huang, M. H. Polyhedral Au-Pd Core-Shell Nanocrystals as Highly Spectrally Responsive and Reusable Hydrogen Sensors in Aqueous Solution. *Angew. Chem., Int. Ed.* **2013**, *52*, 12709–12713.

24. Huang, J.; Zhu, Y.; Lin, M.; Wang, Q.; Zhao, L.; Yang, Y.; Yao, K. X.; Han, Y. Site-Specific Growth of Au-Pd Alloy Horns on Au Nanorods: A Platform for Highly Sensitive Monitoring of Catalytic Reactions by Surface Enhancement Raman Spectroscopy. *J. Am. Chem. Soc.* **2013**, *135*, 8552–8561.

25. Smith, A. F.; Harvey, S. M.; Skrabalak, E.; Weiner, R. G. Engineering High Refractive Index Sensitivity Through the Internal and External Composition of Bimetallic Nanocrystals. *Nanoscale* **2016**, *8*, 16841–16845.

26. Motl, N. E.; Smith, A. F.; DeSantis, C. J.; Skrabalak, S. E. Engineering Plasmonic Metal Colloids Through Composition and Structural Design. *Chem. Soc. Rev.* **2014**, *43*, 3823–3834.

27. Petrova, H.; Perez Juste, J.; Pastoriza-Santos, I.; Hartland, G. V.; Liz-Marzán, L. M.; Mulvaney, P. On the Temperature Stability of Gold Nanorods: Comparison Between Thermal and Ultrafast Laser-Induced Heating. *Phys. Chem. Chem. Phys.* **2006**, *8*, 814–821.

28. Link, S.; Burda, C.; Nikoobakht, B.; El-Sayed, M. A. Laser-Induced Shape Changes of

Colloidal Gold Nanorods Using Femtosecond and Nanosecond Laser Pulses. *J. Phys. Chem. B* **2000**, *104*, 6152–6163.

29. Zijlstra, P.; Chon, J. W. M.; Gu, M. White Light Scattering Spectroscopy and Electron Microscopy of Laser Induced Melting in Single Gold Nanorods. *Phys. Chem. Chem. Phys.* **2009**, *11*, 5915–5921.

30. Taylor, A. B.; Siddiquee, A. M.; Chon, J. W. M. Below Melting Point Photothermal Reshaping of Single Gold Nanorods Driven by Surface Diffusion. *ACS Nano* **2014**, *8*, 12071–12079.

31. Danielsen, S. P. O.; Choi, J.; Composto, R. J. Retardation of Shape Change of Au Nanorods Using Photo-Cross- Linkable Ligands. *J. Polym. Sci., Part B: Polym. Phys.* **2016**, *54*, 301–307.

32. Antonello, A.; Della Gaspera, E.; Baldauf, J.; Mattei, G.; Martucci, A. Improved Thermal Stability of Au Nanorods by Use of Photosensitive Layered Titanates for Gas Sensing Applications. *J. Mater. Chem.* **2011**, *21*, 13074–13078.

33. Albrecht, W.; Deng, T.-S.; Goris, B.; van Huis, M. A.; Bals, S.; van Blaaderen, A. Single Particle Deformation and Analysis of Silica-Coated Gold Nanorods before and after Femtosecond Laser Pulse Excitation. *Nano Lett.* **2016**, *16*, 1818–1825.

34. Albrecht, W.; van der Hoeven, J. E.; Deng, T.-S.; de Jongh, P. E.; van Blaaderen, A. Fully Alloyed Metal Nanorods with Highly Tunable Properties. *Nanoscale* **2017**, *9*, 2845 – 2851.

35. Gergely-Fülöp, E.; Zámbó, D.; Deák, A. Thermal Stability of Mesoporous Silica-Coated Gold Nanorods with Different Aspect Ratios. *Mater. Chem. Phys.* **2014**, *148*, 909–913.

36. Chen, Y.-S.; Frey, W.; Kim, S.; Homan, K.; Kruizinga, P.; Sokolov, K.; Emelianov, S.

Enhanced Thermal Stability of Silica-Coated Gold Nanorods for Photoacoustic Imaging and Image-Guided Therapy. *Opt. Express* **2010**, *18*, 8867–8878.

37. Cao, A.; Veser, G. G. Exceptional High-Temperature Stability Through Distillation-Like Self-Stabilization in Bimetallic Nanoparticles. *Nat. Mater.* **2010**, *9*, 75–81.

38. Zou, R.; Zhang, Q.; Zhao, Q.; Peng, F.; Wang, H.; Yu, H.; Yang, J. Thermal Stability of Gold Nanorods in an Aqueous Solution. *Colloids Surf., A* **2010**, *372*, 177–181.

39. Mohamed, M. B.; Ismail, K. Z.; Link, S.; El-Sayed, M. A. Thermal Reshaping of Gold Nanorods in Micelles. *J. Phys. Chem. B* **1998**, *102*, 9370–9374.

40. Liu, Y.; Mills, E. N.; Composto, R. J. Tuning Optical Properties of Gold Nanorods in Polymer Films Through Thermal Reshaping. *J. Mater. Chem.* **2009**, *19*, 2704–2709.

41. Kennedy, W. J.; Slinker, K. A.; Volk, B. L.; Koerner, H.; Godar, T. J.; Ehlert, G. J.; Baur, J. W. High-Resolution Mapping of Thermal History in Polymer Nanocomposites: Gold Nanorods as Microscale Temperature Sensors. *ACS Appl. Mater. Interfaces* **2015**, *7*, 27624–27631.

42. Midgley, P. A.; Weyland, M. 3D Electron Microscopy in the Physical Sciences: the Development of Z-Contrast and EFTEM Tomography. *Ultramicroscopy* **2003**, *96*, 413–431.

43. Midgley, P. A.; Dunin-Borkowski, R. E. Electron Tomography and Holography in Materials Science. *Nat. Mater.* **2009**, *8*, 271–280.

44. Ersen, O.; Florea, I.; Hirlimann, C. A.; Pham-Huu, C. Exploring Nanomaterials with 3D Electron Microscopy. *Mater. Today* **2015**, *18*, 395–408.

45. Vanrompay, H.; Bladt, E.; Albrecht, W.; Béché, A.; Zakhozheva, M.; Sánchez-Iglesias, A.; Liz-Marzán, L. M.; Bals, S. 3D Characterization of Heat-Induced Mor-

phological Changes of Au Nanostars by Fast *In Situ* Electron Tomography. *Nanoscale* **2018**, *10*, 22792–22801.

46. Aarle, W. V.; Palenstijn, J. W.; De Beenhouwer, J.; Altantzis, T.; Bals, S.; Batenburg, K. J.; Sijbers, J. The ASTRA Toolbox: A Platform for Advanced Algorithm Development in Electron Tomography. *Ultramicroscopy* **2015**, *157*, 35–47.

47. Moon, T. K. The Expectation-Maximization Algorithm. *IEEE Signal Proc. Mag.* **1996**, *13*, 47–60.

48. Albrecht, W.; van de Glind, A.; Yoshida, H.; Isozaki, Y.; Imhof, A.; van Blaaderen, A.; de Jongh, P. E.; de Jong, K. P.; Zečević, J.; Takeda, S. Impact of the Electron Beam on the Thermal Stability of Gold Nanorods Studied by Environmental Transmission Electron Microscopy. *Ultramicroscopy* **2018**, *193*, 97–103.

49. Ringe, E.; DeSantis, C. J.; Collins, S. M.; Duchamp, M.; Dunin-Borkowski, R. E.; Skrabalak, S. E.; Midgley, P. A. Resonances of Nanoparticles with Poor Plasmonic Metal Tips. *Sci. Rep.* **2015**, *5*, 17431.

50. Mejia-Rosales, S. J.; Fernández-Navarro, C.; Pérez-Tijerina, E. Two-Stage Melting of Au-Pd Nanoparticles. *J. Phys. Chem. B* **2006**, *110*, 12884–12889.

51. Pakizeh, T.; Langhammer, C.; Zorić, I.; Apell, P.; Käll, M. Intrinsic Fano Interference of Localized Plasmons in Pd Nanoparticles. *Nano Lett.* **2009**, *9*, 882–886.

52. van der Hoeven, J. E. S.; Welling, T. A. J.; Silva, T. A. G.; van den Reijen, J. E.; La Fontaine, C.; Carrier, X.; Louis, C.; Blaaderen, A. V.; de Jongh, P. E. *In Situ* Observation of Atomic Redistribution in Alloying Gold-Silver Nanorods. *ACS Nano* **2018**, *12*, 8467–8476.

53. Chen, C.-Y.; Li, H.-X.; Davis, M. E. Studies on Mesoporous Materials: I. Synthesis and Characterization of MCM-41. *Microporous Mater.* **1993**, *2*, 17–26.

54. Chang, C.-C.; Wu, H.-L.; Kuo, C.-H.; Huang, M. H. Hydrothermal Synthesis of Monodispersed Octahedral Gold Nanocrystals with Five Different Size Ranges and Their Self-Assembled Structures. *Chem. Mater.* **2008**, *20*, 7570–7574.

55. DeSantis, C. J.; Weiner, R. G.; Radmilovic, A.; Bower, M. M.; Skrabalak, S. E. Seeding Bimetallic Nanostructures as a New Class of Plasmonic Colloids. *J. Phys. Chem. Lett.* **2013**, *4*, 3072–3082.

56. Weiner, R. G.; DeSantis, C. J.; Cardoso, M. B. T.; Skrabalak, S. E. Diffusion and Seed Shape: Intertwined Parameters in the Synthesis of Branched Metal Nanostructures. *ACS Nano* **2014**, *8*, 8625–8635.

57. de la Peña, F.; Ostasevicius, T.; Fauske, V. T.; Burdet, P.; Prestat, E.; Jokubauskas, P.; Nord, M.; Sarahan, M.; MacArthur, K. E.; Johnstone, D. N.; Taillon, J.; Caron, J.; Migunov, V.; Eljarrat, A.; Furnival, T.; Mazzucco, S.; Aarholt, T.; Walls, M.; Slater, T.; Winkler, F. *et al.* hyperspy/hyperspy: HyperSpy 1.3.2. 2018; `https://doi.org/10.5281/zenodo.1304308`.

Graphical TOC Entry